Tuning the ¹O₂ Oxidation of a Phenol at the Air/Solid Interface of a Nanoparticle: Hydrophobic Surface Increases Oxophilicity

Andrés M. Durantini, ¹⁻³ Lloyd Lapoot, ^{1,4} Shakeela Jabeen, ^{1,2} Goutam Ghosh, ^{1,2} Johirul Bipu, ¹ Serah Essang, ^{1,2} Britney C. Singh, ^{1,2} and Alexander Greer ^{1,2,4}*

 $^{\rm 1}$ Department of Chemistry, Brooklyn College, Brooklyn, New York, USA

² Ph.D. Program in Chemistry, The Graduate Center of the City University of New York, New York, New York, USA

³ IDAS-CONICET, Departamento de Química, Facultad de Ciencias Exactas, Físico-Químicas y Naturales, Universidad Nacional de Río Cuarto, Ruta Nac. 36 Km 601, X5804BYA Río Cuarto, Córdoba, Argentina

⁴ Ph.D. Program in Biochemistry, The Graduate Center of the City University of New York,

New York, New York, USA

ABSTRACT

Although silica surfaces have been used in organic oxidations for the production of peroxides, studies of airborne singlet oxygen at interfaces are limited and have not found widespread advantages. Here, with prenyl phenol coated silica and delivery of singlet oxygen (¹O₂) through the gas phase, we uncover significant selectivity for dihydrofuran formation over allylic hydroperoxide formation. The hydrophobic particle causes prenyl phenol to produce an isohydroperoxide intermediate with an internally protonated oxygen atom, which leads to dihydrofuran formation as well as O-atom transfer. In contrast, hydrophilic particles cause prenyl phenol to produce allylic hydroperoxide, due to phenol OH hydrogen bonding with SiOH surface groups. Mechanistic insight is provided by air/nanoparticle interface coated with the prenyl phenol, in which product yield were 6-fold greater on the hydrophobic nanoparticles compared to the hydrophilic nanoparticles and total rate constants (ASI- k_T) of ${}^{1}O_2$ were 13-fold greater on the hydrophobic vs hydrophilic nanoparticles. A slope intersection method (SIM) method was also developed that uses the airborne ${}^{1}O_{2}$ lifetime ($\tau_{airborne}$) and surface-associated ${}^{1}O_{2}$ lifetime (τ_{surf}) to quantitate ¹O₂ transitioning from volatile to non-volatile and surface boundary (surface...¹O₂). Further mechanistic insight on the selectivity of the reaction of prenyl phenol with ¹O₂ was provided by DFT calculations.

INTRODUCTION

Interfacial strategies for selectivity in singlet oxygen (${}^{1}O_{2}$) reactions could be developed which do not rely on compartmentalization effects ${}^{1-4}$ and which also use air-water or air-solid interfaces. One relatively new approach is the delivery of ${}^{1}O_{2}$ as a gas to the air-water interface in

the presence of prenylsurfactants [(CH₃)₂C=CH(CH₂)_nSO₃⁻ Na⁺ (n = 4, 6, 8)], which results in higher 'ene' hydroperoxide regioselectivity for secondary ROOH to tertiary ROOH, which is a relatively new approach.⁵ Five reports have referred to our previous work in seeking selectivity in airborne ¹O₂ reactions; they have further reported on interfacial strategies,⁵⁻⁹ where ¹O₂ arrives top-down as a gas to an air-water interface.

The use of airborne ${}^{1}O_{2}$ and its quenching at an interface can offer selectivity control, but its important application to prenyl phenol (Pr, [2-(3-methylbut-2-en-1-yl)phenol]) has been sparsely researched. Because airborne ${}^{1}O_{2}$ can be generated and arrive to a surface such as a particle, mechanistic processes to control its surface chemistry need to be explored. One paper in 2021 reported on the interparticle delivery and detection of airborne ${}^{1}O_{2}$ at the air-particle interface, where a [4 + 2] cycloaddition to anthracene compounds arose. This previous 2021 work presented a more qualitative aspect with air-solid interface total quenching rate constant (*ASI-k*_T) measurements of ${}^{1}O_{2}$, but with no chemical selectivity observed. Different coatings on particles with varying hydrophobic and hydrophilic properties, could be introduced into the system to potentially bias ${}^{1}O_{2}$ chemistry (Figure 1). Here, we tackle the problem of ${}^{1}O_{2}$ oxidation at the air-particle interface for selective control of a Pr due to oxophobilicty/philicity interactions. The present work which examines the air-particle interface for selective control of a Pr, presents a quantitative approach called the slope intersection method (SIM), along with *ASI-k*_T measurements and accompanying DFT results.

Specifically, our work provides mechanistic insight to selective airborne ¹O₂ chemistry on three fronts: we (1) photogenerated ¹O₂ on a sensitizer particle, which travels through air to a second particle bearing the oxidizable Pr compound. Here, product selectivity and product yields of ¹O₂ are determined on hydrophobic and hydrophilic particles coated with the Pr. Also, air/solid

interface total rate constants ($ASI-k_T$) of 1O_2 are determined on the hydrophobic and hydrophilic particles coated with the Pr. (2) Singlet oxygen can be directly detected by near-IR phosphorescence for its lifetime as an airborne species and as a surface-associated species. The lifetime of singlet oxygen is probed as an airborne species ($\tau_{airborne}$) and at the particle surface (τ_{surf}), in order to determine whether heterogeneous surfaces offer control in sensitized-photooxidation of Pr. The Pr forms either dihydrobenzofuran 1 or allylic hydroperoxides 2 and 3 depending on whether the surface is hydrophobic or hydrophilic. This can be quantitated by 1O_2 quenching of the particle surface coated with Pr. Specifically, SIM is used to assess singlet oxygen transfer characteristics, utilizing quenching and lifetime (τ) data to identify slope inflection parameters to rank 1O_2 over the spectrum from particle-dissociated to -associated species. (3) DFT calculations provided additional mechanistic insight. The results of our work provide evidence for the mechanism shown in Figure 1, wherein particle *a*proticity is revealed, increasing the reactivity of 1O_2 with the prenyl group. DFT data point to the intermediacy of an *iso*-hydroperoxide (**ISO**).

One innovation described in this paper lies in the new air-particle interface detection method. This method, using SIM, provides an intersection angle, which uses the airborne ${}^{1}O_{2}$ lifetime ($\tau_{airborne}$) and surface-associated ${}^{1}O_{2}$ lifetime (τ_{surf}), making the mechanism easy to understand. We justify the choice of material, using silica nanoparticles in an effort to control the ${}^{1}O_{2}$ reaction. Somewhat similarly, control of radical stabilization and photochemical reactions have been obtained on silica nanoparticle. ${}^{11-13}$ We propose that our ${}^{1}O_{2}$ air-solid method could have general applicability in a variety of research areas such as interfacial ${}^{1}O_{2}$ photoimaging 14,15 and environmental chemistry. 16,17 Therefore, we provide a detailed description of SIM, which enables one to gauge $Pr/{}^{1}O_{2}$ adduct binding. This includes how to conduct the airborne and surface-

associated $^{1}O_{2}$ lifetime experiments, while differentiating how $^{1}O_{2}$ plays important roles in oxidizing particulates $^{18-21}$ with intermediacy on surfaces 22,23 and in air. 24,25

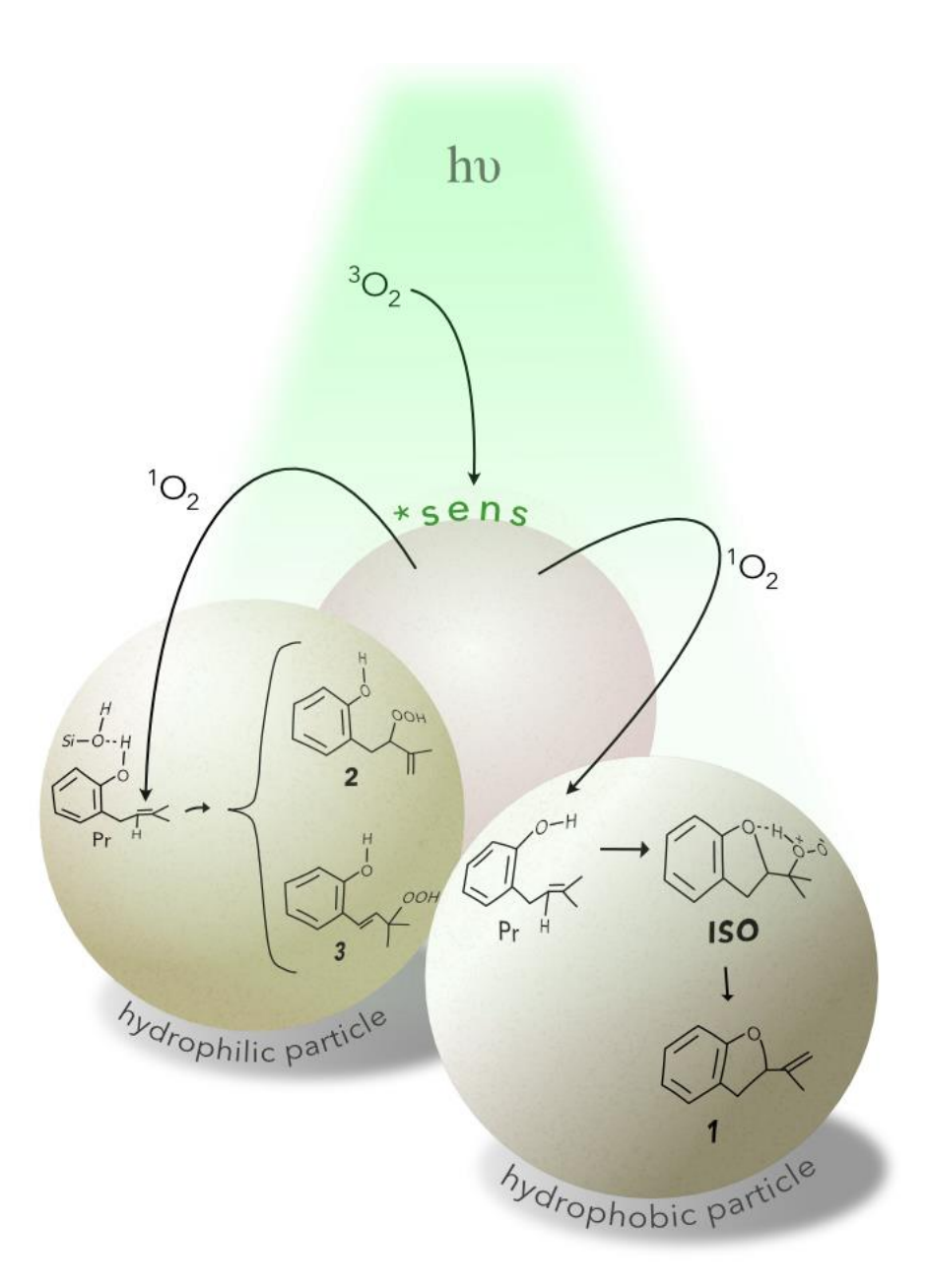


Figure 1. Schematic showing the irradiation of the photosensitizer particle (P_{PS}), formation of airborne singlet oxygen (¹O₂), and its interaction with prenyl phenol (Pr) coated on hydrophobic (P_{SiMe}) or hydrophilic particles (P_{SiOH}). Regioselectivity is found leading to dihydrofuran **1** by an

iso-hydroperoxide intermediate (**ISO**) on P_{SiMe} particles, whereas a $^{1}O_{2}$ 'ene' reaction leads to allylic hydroperoxides 2 and 3 on the P_{SiOH} particles.

MATERIALS AND METHODS

General. The following reagents were purchased from Sigma-Aldrich and used as received: 3,3-dimethylallyl bromide, sodium hydride, sodium bicarbonate, sodium sulfate, sodium nitrite, phenol, and HPLC-grade acetonitrile. Diethyl ether, ethyl acetate, hexanes, H₂O₂ (3 w/v%), toluene (anhydrous), CHCl₃, CDCl₃, and DMSO-d₆ were purchased from VWR and used as received. Aluminum (III) phthalocyanine dichloride (AlPcCl₂) was purchased from Frontier Scientific and used as received. Prenyl phenol (Pr)²⁶ and 8-acetoxymethyl-2,6-dibromo-1,3,5,7tetramethyl pyrromethene fluoroborate (Br₂B-OAc)²⁷ were synthesized based on literature procedures. CAB-O-Sil TS-720 fumed silica (surface-treated with polydimethylsiloxane, average diameter: 250 nm, surface area: $200 \pm 25 \text{ m}^2/\text{g}$) and S5505 hydrophilic fumed silica (surface area: average diameter: 250 nm, 200 ± 25 m²/g and ~4 silanol groups/nm²) was purchased from Composite Resources (Rock Hill, SC). Silica gel particles (average diameter: 60 µm) were purchased from SiliCycle® Inc. Porous Vycor glass (PVG) was used (Corning 7930 from Advanced Glass and Ceramics, Holden, MA, density is 1.38 g/mm³) and ground into microparticles with an average diameter of 69 µm. A Brucker Avance 400 MHz instrument was used to collect ¹H NMR data. A Nicolet iS10 FTIR instrument was used to collect IR data. The three photolysis apparatuses that were used are shown in Figure 2A-C and are described below.

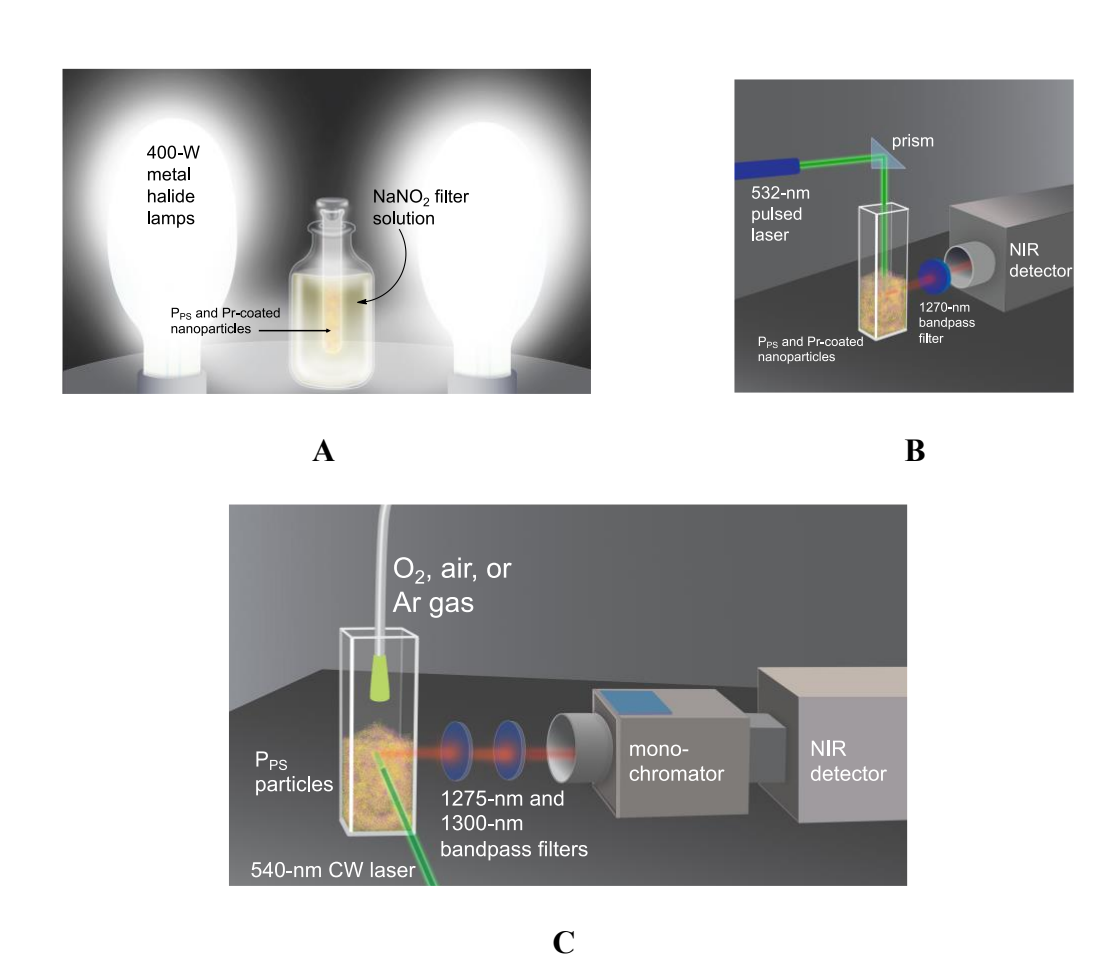


Figure 2. Photolysis apparatuses used in the product studies (A), time-resolved studies (B), and ${}^{1}\text{O}_{2}$ phosphorescence measurements (C).

Airborne ¹O₂/Pr Nanoparticle Reactions: Product Studies. Photosensitizer particles (P_{PS}) were prepared with a loading Br₂B-OAc or Al(III)Cl₂Pc was adsorbed onto PVG particles in a manner similar to that previously described. ¹⁰ Here, Br₂B-OAc or Al(III)Cl₂Pc (0.20 μmol) was dissolved in 3.0 mL CHCl₃ and stirred with 100 mg of PVG particles for 3 min. The CHCl₃ was then evaporated at low pressure at low pressure with a rotary evaporator leaving the sensitizer adsorbed. Pr was adsorbed onto either hydrophobic and hydrophibic nanoparticles. Pr (200 μmol) was dissolved in 6.0 mL CHCl₃ and stirred with 100 mg of hydrophobic fumed for 3 min. The

CHCl₃ was then evaporated at low pressure with a rotary evaporator leaving the Pr adsorbed. Airborne $^{1}\text{O}_{2}$ reactions with Pr on hydrophobic and hydrophilic nanoparticles were carried out in 5-mL test tube. The P_{PS} nanoparticles and the hydrophobic or hydrophilic nanoparticles coated with Pr were mixed. The particles were stationary during the 1-h irradiation period, where the test tube containing the particles was placed inside of a 1-cm NaNO₂ filter solution (75 w/v%) to block light < 400 nm. The samples were irradiated with two 400-W metal halide lamps in which the photons (400 < λ < 700 nm) were absorbed by P_{PS} (Figure 2A). During the irradiation period, the temperature rose less than by ~3 °C. For the NMR studies, after photolysis, compounds were desorbed from the hydrophobic or hydrophilic nanoparticle surfaces by stirring with 6-mL CHCl₃ for 3-5 min. No filtering of the sensitizer particles away from the Pr-coated particles because of the very low amount of the sensitizer used (PS:Pr = 1:1000). Particles in the CHCl₃ were removed passing through a syringe filter. CHCl₃ was evaporated and replaced with CDCl₃. For the IR studies, after photolysis, the compounds were analyzed directly on the nanoparticle surfaces.

Airborne 1 O₂/Pr Nanoparticle Reactions: Time-Resolved Studies. A particle device was used as described previously. 10 P_{PS} particles were prepared with a loading 0.05 μmol Br₂B-OAc/g (7.1 × 10⁹ PS molecules/PVG particle) or 0.05 μmol Br₂B-OAc/g (6.8 × 10⁹ PS molecules/60 μm silica gel particle). The particles were loaded with Pr (0 up to 200 μmol/g) (0 to 2.3×10^9 Pr molecules/ fumed particle). Experiments were carried out in a cuvette filled with P_{PS} (100 mg, 7.1×10^9 PS molecules/PVG particle and Pr-loaded particles (100 mg, 0-2.3 × 10⁸ Pr molecules/fumed silica particle) for net ratios PS:Pr of 65:1, 25:1, 13:1, 6:1, and 1:3. The number of P_{SiMe} or P_{SiOH} is 5.3×10^{10} particles/g and the weight of each particle is 1.9×10^{-8} mg, each accurate to ±2%. The number of PS particles in each experiment was 4.2×10^6 particles, and the weight of each particle is 2.4×10^{-7} g.

Quenching of Airborne ¹O₂ by Pr at the Air/Particle Interface. The ¹O₂ photosensitizing nanoparticles (P_{PS}) were prepared adsorbing 0.05 µmol of Br₂B-OAc sensitizer per gram of PVG, which was previously found to be the optimal loading as reflected in the longest lifetime for ¹O₂ in air (Figure 2B). ¹⁰ To monitor ¹O₂ phosphorescence, 100 mg of P_{PS} particles was mixed with 100 mg of nanoparticles containing the desired loading of prenyl phenol. To acquire the kinetic traces, the samples were irradiated with an Nd:YAG Q-switched laser operating at 5 Hz. The optical layout was configured to produce 532 nm, 5 Hz, and 30 mJ/pulse. The excitation of the nanoparticle samples was irradiated from the top. There is no solvent in the system, oxygen is from air as a static source surrounding the nanoparticles. The ¹O₂ phosphorescence was detected employing a photomultiplier tube (H10330A-45 Hamamatsu Corp.) in which the emitted light was detected through a NIR band-pass filter centered at 1270 nm (OD4 blocking, FWHM = 15 nm). Our particle system is static. Basic calculations show the diffusion time and length scale (L^2/D) to be shorter than the kinetic τ . For example, $L^2/D < \tau$ (L^2/D for 1 nm up to 50 μ m has mass transport times of 5×10^{-14} s up to 1.2×10^{-4} s, respectively, which are shorter compared to our measured $\tau_{airborne}$ of 5.5 \times 10⁻⁴ s), see the time-resolved results below, using a diffusion coefficient for oxygen in air of 1.98×10^{-5} m² s⁻¹.²⁸ Notably, the τ of ¹O₂ is shorter in quencher-free H₂O (3.5 μ s).²⁹ In our system, a kinetic model can be used for the data gathered, in which a number of collisions of ¹O₂ with Pr are required prior to a chemical reaction as it is not a diffusion controlled bimolecular reaction. To acquire the intensity vs time trajectories the same instrumentation described above was used, but now the samples were excited from the top and not on one face of the cuvette. The decay curves were fitted with a biexponential function (eq 1) where I is the intensity at any given point in time, I_0 is the intensity when $t = \infty$, t is the time, τ_{surf} is the observed lifetime 1 (short component, attributed to ${}^{1}O_{2}$ on the surface of the particles) and $\tau_{airborne}$ is the observed lifetime 2

(long component, assigned to ${}^{1}O_{2}$ in the air), and A is the amplitude. A values in A_{surf} and A_{airborne} are the amplitudes or the pre-exponential factors, and correspond to the number of airborne ${}^{1}O_{2}$ molecules.

$$I = I_0 + A_{\text{surf}} e^{-t/\tau_{\text{surf}}} + A_{\text{airborne}} e^{-t/\tau_{\text{airborne}}}$$
(1)

The quenching of ${}^{1}O_{2}$ phosphorescence emission by the particles containing Pr is given by eq 2 that is a derivation of the Stern-Volmer analysis. We emphasize that $\tau_{airborne}$ is greater than τ_{surf} , and since τ_{surf} are small values throughout the experiments, and particles containing the quencher deactivates mainly airborne ${}^{1}O_{2}$, eq 2 is expressed as a function of $\tau_{airborne}$,

$$\frac{\tau_0}{\tau_{\text{airborne}}} = 1 + (ASI - k_T)\tau_0[Pr]$$
 (2)

where τ_0 corresponds to the lifetime of ${}^1{\rm O}_2$ in air and $ASI-k_{\rm T}$ is the air/solid interface total quenching rate constant. The ASI- $k_{\rm T}$ values were determine using only the long times ($\tau_{\rm airborne}$) obtained by fitting with a biexponential function. This is done also based on our previous control reactions using the same photosensitizer particles to study the oxidation of an aromatic compound, 10 which showed that removing O_2 via an N_2 purge and using physical and chemical $^{1}O_2$ quenchers pointed to $\tau_{\rm airborne}$ as the lifetime of airborne $^{1}O_2$. Considering that $k = 1/\tau$ eq 2 can also be expressed as:

$$k_{\text{airborne}} = k_{\text{d}} + (ASI - k_{\text{T}})[Pr]$$
 (3)

In this eq, $k_{airborne}$ is the observed rate constant for airborne ${}^{1}O_{2}$, k_{d} is the rate constant of deactivation of ${}^{1}O_{2}$ by air, and Q is the prenyl phenol quencher. OriginPro (Academic, version 8.5.1, OriginLab Corporation, Northampton, MA, USA) was used to plot data, including an extension Tangent.opx from OriginLab Corporation as an add-on tool called "Estimate Onset of Slope".

Slope Intersection Method (SIM). Figure 3 shows the τ_{Δ} decay profiles of ${}^{1}O_{2}$ in the airborne state (A), at the particle surface (C), and the segue between the two (B). For (B), θ is determined by the law of cosines shown in eq 4:

$$\theta = \cos^{-1} \frac{C^2 - B^2 - A^2}{2 A C} \tag{4}$$

where A, B, and C correspond to the sides of an obtuse triangle. To obtain θ , the three slopes (sides) were calculated with eqs 5-7 and the use of Pythagoras theorem. Here, P₁, P₂, and P₃ are the points or corners opposite to sides C, A, and B, respectively. The position for these points is provided by the X and Y coordinates in the plot enabling the solution to these equations.

$$A = P_1 - P_3 = \sqrt{(X_1 - X_3)^2 + (Y_1 - Y_3)^2}$$
 (5)

$$B = P_1 - P_2 = \sqrt{(X_1 - X_2)^2 + (Y_1 - Y_2)^2}$$
 (6)

$$C = P_2 - P_3 = \sqrt{(X_2 - X_3)^2 + (Y_2 - Y_3)^2}$$
 (7)

To obtain the coordinates, four points were selected on the intensity decay curve (Figure 3, vertical red lines 1-4). Then, the Y values of the curve were automatically computed at these four positions by interpolation. After designating the position of lines 1-4, lines A and C were generated by connecting the X and Y points, with the intersection yielding the coordinates for point P_1 . In Figure 3, vertical lines 3 and 4 are used to bracket the short decay and vertical lines 1 and 2 are used to bracket the long decay. Our technique was found to be reasonably accurate to within $\theta \pm 0.5^{\circ}$. Selection of the points along the intensity decay curve were kept constant for all the experiments with values of 5×10^{-5} , 1×10^{-4} , 5×10^{-4} , and 8×10^{-4} s for lines 3, 4, 1, and 2,

respectively. The choice of these values was based in the following assumption: since the intensity decay trajectories are bi-exponential and the analysis implies linear interpolation, with these values the maximum overlap between the fast and slow component of the decay and computed lines A and C was achieved.

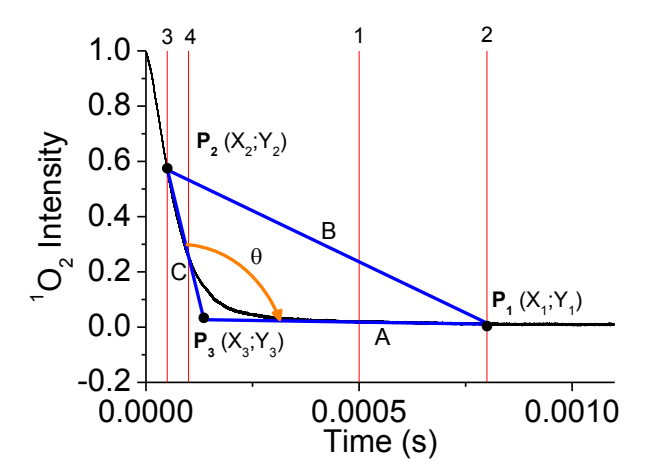


Figure 3. Slope intersection method (SIM): A representative decay profile of ${}^{1}O_{2}$ in air (A) and being quenching by Pr at the particle surface (C), and deduction of the point straddling the two (B). Blue lines A, B, and C represent the slope and the intersections define the X and Y axes for points P₁, P₂, and P₃, from where the value for θ is obtained. The vertical red lines across the plot denote the points selected to define lines A and C.

Further ¹O₂ phosphorescence measurements were also carried out on a second laser system consisting of a HORIBA Fluorolog-QM spectrofluorometer (Figure 2C). Here, a photomultiplier tube (H10330A-45 Hamamatsu Corp.) similar to that above was also used, but it was coupled to the spectrofluorometer and a supercontinuum pulsed laser (SuperK Fianium FIU-15 provided by NKT Photonics) was used as the excitation source. Two-band pass emission filters

(1300/200 nm and 1275/30 nm) were used to minimize scattered light. The laser was controlled using two external radiofrequency (RF) drivers from NKT Photonics. The excitation rate was 78.1 MHz, and the power was 0.5 mW at 540 nm. A home built triangular 3D-printed mini-cuvette was used for the solid samples. The photosensitizer particles were tightly packed in the sample holder of the cuvette and supported with a glass coverslip. The plastic cuvette with the sample was then fitted into a conventional ($10 \times 10 \text{ mm}$) glass cuvette and sealed with a septum allowing to purge the sample with Ar (10 min), O_2 (30 min), and to apply vacuum (1 h) using an oil vacuum pump.

Computational Section. We carried out optimizations, frequency calculations, and intrinsic reaction coordinate (IRC) calculations using the Gaussian16 program (revision C.01)³⁰ along with Gaussview 6.0 for visualizations.³¹ Calculations were performed with B3LYP in conjunction with the basis set 6-31G+(d,p). The energies are reported as enthalpies with thermal corrections to 298 K. Frequency and IRC calculations were carried out to verify transition state (TS) structures. We find that *iso*-hydroperoxide 3 is a minimum based on B3LYP/6-31G+(d,p) calculations, which was then used in a single point CCSD(T)/6-31+G(d,p) calculation via Gaussian16 to examine for possible spin contamination via Lee and Taylor's T1 diagnostic test.³² Estimated distances between Pr molecules on the fumed particle surface were estimated by optimizing the Pr geometry with the MMFF force field using Avogadro software (version 1.2.0).³³

RESULTS AND DISCUSSION

Airborne ¹O₂/**Pr Nanoparticle Reactions: Product Studies.** The reaction of airborne ¹O₂ with Pr on hydrophobic and hydrophilic nanoparticles led to products **1-3**, and **5** according to NMR following their desorption (Table 1). The nanoparticle type was found to bias the product outcome.

On hydrophobic nanoparticles, dihydrobenzofuran 1 was the main product, along with epoxide 5, along with trace amounts of hydroperoxides 2 and 3. On hydrophilic nanoparticles, the amount of hydroperoxides 2 and 3 increased and the amount of dihydrobenzofuran 1 decreased, and epoxide 5 was not detected. A ratio of dihydrobenzofuran 1 to the hydroperoxides 2 and 3 on the hydrophobic nanoparticles is ~20:1, but on the hydrophilic nanoparticles is 0.2:4.0. This amounts to a ~85-fold increase in dihydrobenzofuran 1 formation on hydrophobic nanoparticles compared to hydrophilic nanoparticles. We found that the ratio of hydroperoxides 2:3 does not depend on the hydrophobic or hydrophilic nanoparticle surface, where the ratio of the two remained near to ~1:1. A note on the stability the hydroperoxides 2 and 3 on the nanoparticle surfaces, we find that after a few days the surface led to a decrease of 3, with formation of by-product methane that is consistent with this pointing to its formation by a decomposition of a *gem*-dimethyl alkoxy radical of 3. On the hydrophobic nanoparticles, we detected the formation of the epoxide 5, but not on the hydrophilic nanoparticles.

Table 1. Effect of hydrophobic and hydrophilic nanoparticle surfaces on the product ratios in the reaction of airborne ${}^{1}O_{2}$ with Pr. a

	hydrophobic	hydrophilic	
products	nanoparticle nanoparticle		
	(P _{SiMe})	(Psioh)	
dihydrobenzofuran 1	17 0.2		
hydroperoxide 2	0.5	2.1	
hydroperoxide 3	eroxide 3 ~0.2 1.9		

epoxide **5** 9 0

^a Relative yields averaged from photosensitizer particles P_{PS} (Br₂B-OAc or Al(III)Cl₂Pc), where in ¹H NMR product peaks were consistent with those reported in literature.³⁴ Hydroperoxides **2** and **3** are stable up to 2-3 days on the nanoparticles. Information on the quantitation of H₂O₂ is not included as it was found not to be reliable by NMR.

Airborne ¹O₂/Pr Nanoparticle Reactions: Time-Resolved Studies. Results were obtained for air/solid interface total rate constants (ASI-k_T) of ¹O₂ by hydrophobic and hydrophilic nanoparticles loaded with the Pr. The setup consisted of PVG particles coated with a Br₂B-OAc photosensitizer (P_{PS}) to produce airborne ¹O₂, leading to distinct biexponential intensity decay curves assigned to two lifetimes. The longer lifetime ($\tau_{airborne} \sim 550 \mu s$) was attributed to the ${}^{1}O_{2}$ that diffuses in the air, and the short component ($\tau_{\text{surf}} \sim 60 \,\mu\text{s}$) corresponds to $^{1}\text{O}_{2}$ on the surface of the particle loaded with Pr. The ASI-k_T values of ¹O₂ are the long lifetime component for Pr loaded onto hydrophobic and hydrophilic nanoparticles. Pps particles were mixed in equal weight with hydrophobic (P_{SiMe}) or hydrophilic (P_{SiOH}) nanoparticles, in which intensity vs time trajectories for deactivation of ¹O₂ are shown in Figure 4. Here, the time window is sufficiently large for ample detection of the long-time signal. The intensity diminishes with increased loading of Pr on the P_{SiMe} (Figure 4A) and P_{SiOH} (Figure 4B) nanoparticles. Table 2 shows the $\tau_{airborne}$ values when no Pr is adsorbed of 725 and 697 µs for P_{SiMe} and P_{SiOH}, respectively. These values in Table 1, entry 1 are similar to those obtained from the Y-axis intercepts in Figure 4A and 4B of $\tau_0 = 693 \mu s$ for P_{SiMe} and $\tau_0 = 700$ us for P_{SiOH} . These lifetimes of airborne ${}^{1}O_2$ are near to that of 0.98 ms of ${}^{1}O_2$ in gas bubbles, 35 where longer lifetimes have also been reported under turbulent flow, pressure gradient, or other condition.³⁶⁻⁴¹ Increasing the loading of Pr up to 200 µmol per gram nanoparticles showed a reduction of the lifetime that was strongly influenced by the hydrophobicity of the nanoparticle. Namely, increased Pr loading on the hydrophobic nanoparticles showed a 7-fold decrease in the $\tau_{airborne}$ values, where for hydrophilic nanoparticles bearing SiOH groups, the decrease was only 1.4-fold. Fitting of the data in Figure 5 with eq 3 allowed to obtain the values for $ASI-k_T$ of 4.2×10^7 g mol⁻¹ s⁻¹ for P_{SiMe} (Figure 5A) and 3.1×10^6 g mol⁻¹ s⁻¹ for P_{SiOH} (Figure 5B) (Table 3). Furthermore, Figure S7 (Supporting Information) shows phosphorescence spectra of 1O_2 of the P_{PS} under different conditions including purging with O_2 , air, and Ar gas or under vacuum. To gain further insight to the 1O_2 reaction with Pr on the nanoparticle surfaces, a slope intersection method was developed, as described next.

Table 2. Lifetime measurements of ${}^{1}O_{2}$ by direct phosphorescence at 1270 nm as an airborne species ($\tau_{airborne}$) and on the particle surface (τ_{surf}) with associated slope intersection angles (θ) at different particles loading of prenyl phenol (Pr).

entry	Pr loading P _{SiMe}			PsioH			
•	(µmol/g)	$ au_{\text{surf}} (\mu s)^b$	τ _{airborne} (μs) ^b	Θ^c	$\tau_{\text{surf}} (\mu s)^b$	τairborne (μs) ^b	$\mathbf{\theta}^{c}$
1	0^a	55	725	99.2	53	697	98.9
2	10	53	559	97.2	52	680	98.4
3	25	54	382	95.1	53	670	98.0
4	50	54	278	94.3	49	630	97.7
5	100	53	191	94.0	48	580	97.5
6	200	52	104	93.2	47	486	97.3

^a P_{PS} particles were mixed with P_{SiMe} or P_{SiOH} particles in a 1:1 ratio. ^b Errors for τ_{surf} and $\tau_{airborne}$ are ±1 and ±5-10 μs, respectively, and errors for the fittings were 0.01-0.03 μs. ^c Errors for θ based on the slopes analysis are ± 0.5°, and thus we favor this method. A digital protractor method was also used in which the long lifetime line started at $t = \infty$ (I = 0) and ended in the intersection with the descending line. However, we found that the obtuse angle between the two lines by the digital protractor was less reliable, with error in θ > 2.0°.

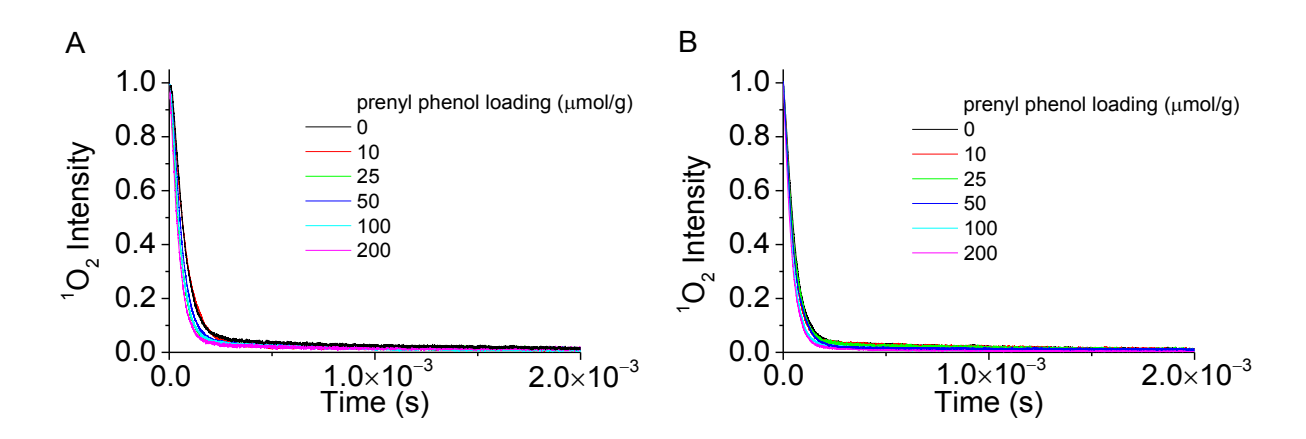


Figure 4. Normalized ¹O₂ luminescence decay curves monitored at 1270 nm for mixtures of (A) P_{PS}:P_{SiMe} (1:1) and (B) P_{PS}:P_{SiOH} with increasing loadings of prenyl phenol (Pr).

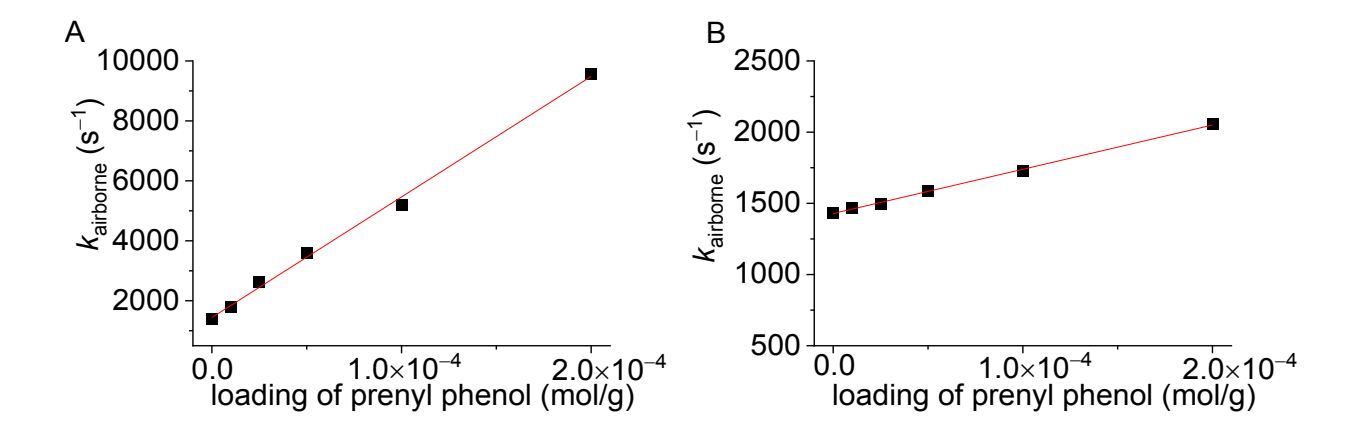


Figure 5. Plots of k_{airborne} (s⁻¹) as a function of the moles of prenyl phenol (Pr) loaded per gram of (A) hydrophobic and (B) hydrophilic nanoparticles.

Table 3. Total quenching rate constant (k_T) measurements of ${}^{1}O_2$ by prenyl phenol (Pr) at the air/nanoparticle interface.

Medium	solid support	heterogeneous $ASI-k_{\rm T}~({\rm g~mol^{-1}~s^{-1}}) \times 10^7$		
	hydrophobic			
	nanoparticles			
	(PsiMe)	4.2 ± 0.1		
air/particle				
interface	hydrophilic			
	nanoparticles	0.21 + 0.00		
	(P_{SiOH})	0.31 ± 0.08		

Slope Intersection Method (SIM): Reaction of Airborne ¹O₂ with Pr-Coated Particles.

Shown in Figure 6 are the ${}^{1}O_{2}$ intensity vs time profiles with airborne ${}^{1}O_{2}$ being quenched by Pr on P_{SiMe} and P_{SiOH} particles. Figure 6 shows the lifetime decay for long component of airborne ${}^{1}O_{2}$ ($\tau_{airborne}$) in A and short decay component of ${}^{1}O_{2}$ at the particle surface (τ_{surf}) in C, in which we measure the slope intersection angle θ between the two. With the use of eq 5-7, Table 2 shows that θ decreases upon increased loading of the Pr on the particle. Specifically, when the loading of Pr increased from 0 to 200 µmol/g on the hydrophobic particles, θ decreased 6.0° while a decrease of only 1.6° was observed on the hydrophilic particles. τ_{surf} remains nearly constant upon increased

loading of Pr (varying by 2.6 µs for P_{SiMe} and 5.7 µs for P_{SiOH}), suggesting that the magnitude of θ is mainly determined by the $\tau_{airborne}$. Indeed, increasing the Pr loading reduced both the $\tau_{airborne}$ and θ , with the latter in an L-shape manner (Figure 7A). Figure 7A shows a notable difference in θ vs loading profiles depending on the quencher, Pr. A larger decrease in θ is seen in P_{SiMe} at low content of Pr (0 to 25 µmol/g) that continues above 25 µmol/g and decreased gently and reaches the horizontal part of the "L" toward the higher loadings. In contrast, particles loaded with PsioH show only a modest slope that gradually decreases on higher loading, up to 50 µmol/g. Furthermore, the variation in θ ($\Delta\theta = \theta_{0 \mu mol/g} - \theta_{200 \mu mol/g}$) is ~70% in the first three points for P_{SiMe} particles and ~50% for P_{SiOH}. We note that the data are accurate to ±5.1%. Also, control experiments demonstrated the necessity of light, oxygen and of PPs and Pr loaded onto PsiMe and Psioh. Further insight was sought by calculating the spatial separation of Pr molecules, SiOH and methylsilane surface sites (Table S1, Supporting Information), and yields to help understand quenching of ¹O₂ at the air/particle interface. Tellingly, P_{SiOH} but not P_{SiMe}, contains particle silanol groups that can H-bond to the prenyl phenol OH group. At all loadings of Pr, a lower θ value is observed with P_{SiMe} than P_{SiOH}, where on average the Pr interacts with about 2 SiOH groups on the loading in which ¹O₂ quenching is greater in the latter. Because DFT calculations can also provide insight to H-bonding, next we discuss molecular H-bonding relating to the formation and fate of a so-called *iso*-hydroperoxide **B** in the context of Pr's consumption.

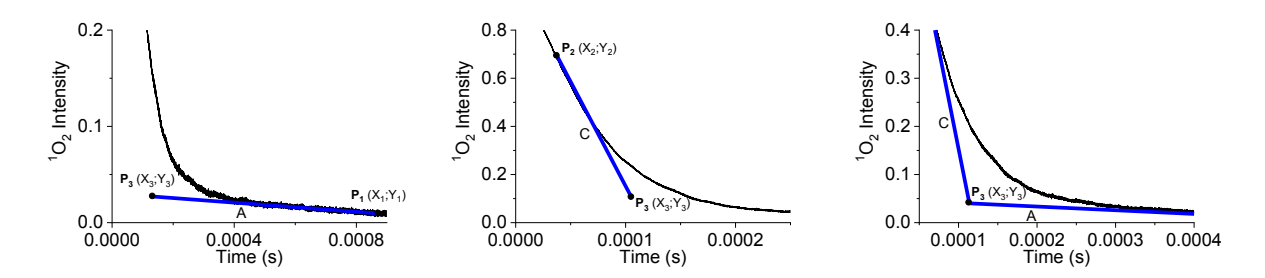


Figure 6. The ${}^{1}O_{2}$ phosphorescence decays shown here are attributed to partitioning of ${}^{1}O_{2}$ from the air to the particle surface. Zoom-in of the lifetime decay for long component of airborne ${}^{1}O_{2}$ ($\tau_{airborne}$) in A; short decay component of ${}^{1}O_{2}$ at the particle surface (τ_{surf}) in C; and slope intersection angle θ between the two.

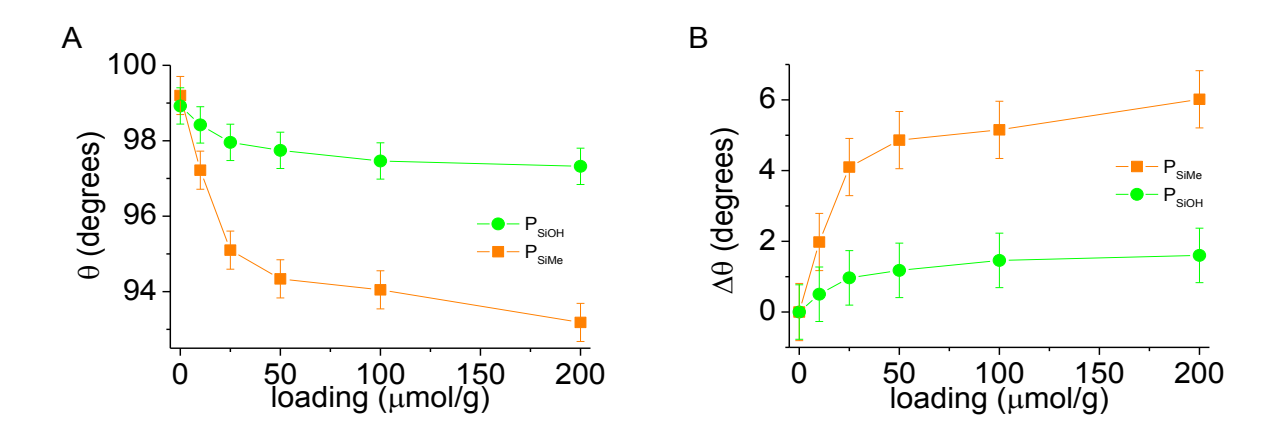


Figure 7. (A) Slope intersection angles (θ) as a function of the prenyl phenol (Pr) quencher loaded on hydrophilic (P_{SiOH}) and hydrophobic (P_{SiMe}) particles. (B) Difference between θ for P_{SiOH} or P_{SiMe} = 0 μ mol/g and P_{SiOH} or P_{SiMe} > 0 μ mol/g, respectively.

Proposed Mechanism and DFT Calculated Results. Singlet Oxygen Directed to the Prenyl Site by the Phenol OH Group. Figure 8i shows the interaction of ${}^{1}O_{2}$ at the particle surface with Pr to form an *iso*-hydroperoxide (**ISO**, also referred to as **B**) and **1** on a hydrophobic surface treated with polydimethylsiloxane, whereas Figure 8ii shows that hydrophilic particles bearing SiOH groups lead to ${}^{1}O_{2}$ 'ene' reactions with formation secondary allylic hydroproxide **2** and tertiary allylic hydroproxide **3**. Figure 8iii shows that Pr is distinguished by the presence or the absence (Pr') of a phenol O–H--- π bond with the prenyl C2'=C3'. The hydrogen of O3'–H is located nearby at a H---C2' distance of 2.215 Å for Pr, but further away at 4.285 Å for Pr', for an NBO calculated O–H--- π interaction of 4.46 kcal/mol in the former. Addition of ${}^{1}O_{2}$ to Pr leads to an

unsymmetrical perepoxide **A** with an O1–C2′ bond distance of 1.543 Å, an O1–C3′ bond distance of 1.623 Å, and relatively linear O–H---O2 bond angle of 176.6°. Pr′ can undergo an 'ene' reaction with $^{1}O_{2}$ to form the allylic hydroperoxides **2** and **3**, but was not studied here, as the $^{1}O_{2}$ 'ene' reaction has been the subject of other detailed computational studies. $^{5,42-44}$ We find that perepoxide **A** resides in a shallow minimum bearing an intramolecular phenol H-bond. Our studies were then focused on the facile routes to the *iso*-hydroperoxide **B** and dihydrofuran **1** (Figure 8iv). Instead of path B leading to hydroperoxide **4**, the formation of dihydrofuran **1** is computed to arise by path A in H₂O₂ expulsion of *iso*-hydroperoxide **B** via **TSB/1**. The activation barrier of **TSB/1** is 6.3 kcal/mol in the gas-phase, where the transition state has an O–C bond distance of 2.008 Å and H–O1–O2–H dihedral angle of -95.1°, thereby releasing H₂O₂. An 90° angle is preferred for free HOOH, where dihedral angle increases lead to enhanced lone-pair interactions on adjacent oxygen atoms. This is known to be destabilizing from antibonding overlap in the π^* molecular orbital, which can reduce the oxygen-oxygen bond energy.

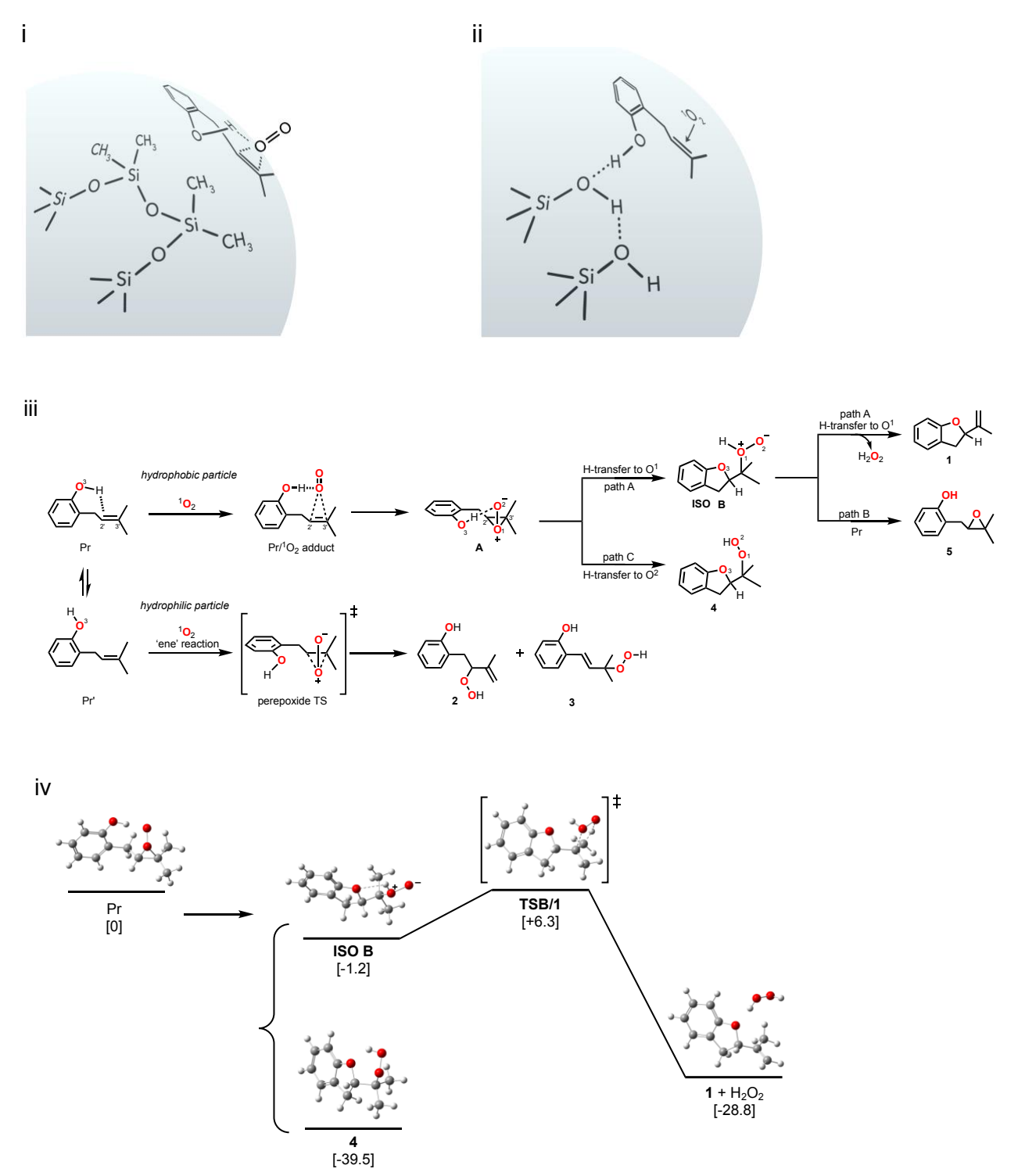


Figure 8. Proposed mechanism and computational results. (i) Interaction of airborne ¹O₂ with the prenyl phenol (Pr) on hydrophobic (P_{SiMe}) or hydrophilic particles (P_{SiOH}) to account for the higher *ASI-k*_T values in the former. (ii) Phenol OH hydrogen bond assisted ¹O₂ oxidation of Pr on P_{SiMe}

with the formation of an *iso*-hydroperoxide **B** leading to dihydrobenzofuran **1**, and (iii) ${}^{1}O_{2}$ 'ene' reaction on P_{SiOH} leads to **2** and **3**. (iv) B3LYP/6-31+G(d,p) calculated potential energy surface for the reaction of ${}^{1}O_{2}$ with Pr to reach **1** and $H_{2}O_{2}$, in which gas-phase energetics are shown in kcal/mol.

Further Mechanistic Considerations. The above results are rationalized in the mechanism shown in Figures 1 and 8, and as follows. After photogeneration of ${}^{1}O_{2}$ on the P_{PS}, airborne ${}^{1}O_{2}$ diffuses and reacts with the Pr on a second particle surface. We found that (i) a 6-fold increase in product yield on the hydrophobic nanoparticles compared to the hydrophobic nanoparticles. Somewhat similarly, the *ASI-k*_T of airborne ${}^{1}O_{2}$ with Pr on the hydrophobic nanoparticles is 13.5-fold greater than on the hydrophilic nanoparticles. Both the product data and *ASI-k*_T data point to molecular H-bonding of Pr with ${}^{1}O_{2}$ can arise on the hydrophobic nanoparticles, but not hydrophilic nanoparticles. Physical quenching by the SiOH groups on the hydrophilic particle was not prevalent, otherwise the opposite trend with a high *ASI-k*_T value would have been observed. Consequently, selectivity favors dihydrofuran 1 over the 'ene' hydroperoxides 2 and 3. A recent report³⁴ also found selectivity, but by homogeneous solvent on product formation, where in C₆D₆, dihydrofuran 1, whereas in CH₃OH the dihydrofuran 1 decreased and amounts of allylic hydroperoxides 2 and 3 increased.

(ii) Our present study focused on a new method to analyze ${}^{1}O_{2}$ phosphorescence data termed "slope intersection method" (SIM). SIM utilizes the concept that a change in slope is due to ${}^{1}O_{2}$ partitioning from the gas phase to the solid phase. We found that the more the Pr was loaded on P_{SiMe} and P_{SiOH} , the more the slope intersection θ decreased, with a concurrent decrease in

 τ_{airborne} , but leaving τ_{surf} mostly unchanged. What is the physical meaning of θ ? When airborne $^1\text{O}_2$ yielded $\theta = 91^\circ$ it is interpreted as increased association of $^1\text{O}_2$ on the surface, whereas 99° represents a weaker association of $^1\text{O}_2$. Greater $\Delta\theta$ reflect increased association at the surface; this is shown in eq 8 in which $\Delta\theta$ is 6.0° varying from $\theta = 99.2^\circ$ to 93.2° on hydrophobic nanoparticles with formation of an **ISO B** intermediate. This is contrasted to a more loosely bound perepoxide transition state with a reduced $\Delta\theta = 1.6^\circ$ varying only from $\theta = 98.9^\circ$ to 97.3° on hydrophilic nanoparticles in eq 9.

PsiMe: [airborne
$${}^{1}O_{2} \stackrel{\mathsf{le}}{\to} (Pr surface \cdots {}^{1}O_{2}) \to ISO B intermediate] \to 1 + 5$$
 (8)

P_{SiOH} [airborne
$${}^{1}O_{2} \stackrel{\mathsf{le}}{\hookrightarrow} (Pr surface \cdot {}^{1}O_{2} \stackrel{\mathsf{le}}{\hookrightarrow} Pr surface \cdot {}^{1}O_{2} \stackrel{\mathsf{le}}{\hookrightarrow} Pr surface \cdot {}^{1}O_{2}) \rightarrow perepoxide TS] \rightarrow 2 + 3 (9)$$

Airborne ${}^{1}O_{2}$ quenching by Pr-loaded particles was greater compared to an uncoated particle. This is due to the chemical quenching and photooxidation of Pr. Figure 7 shows that $\Delta\theta$ increases upon increased Pr loading, when P_{SiMe} or $P_{SiOH} > 0$ µmol/g. That the $\tau_{airborne}$ is shorter with τ_{surf} remaining constant or only slightly decreasing was quite informative. Thus, a theoretical question came to mind: What are the theoretical limits of θ ? If all ${}^{1}O_{2}$ were quenched by Pr at the surface, θ would be 90° . On the other hand, if there was no particle quenching, θ would be 180° , which would signify that the lifetime of ${}^{1}O_{2}$ is the same as a gaseous species and surface-adsorbed species. The absence of surface ${}^{1}O_{2}$ quenching would theoretically lead to τ_{surf} becoming equivalent to $\tau_{airborne}$. In the present study, however, a reasonable notion for the shorter lifetime on coated particles is enhanced participation of Pr in chemical quenching, whereby there is less participation by SiO–H vibrational deactivation in the physical quenching of ${}^{1}O_{2}$. Evidence in (i)

and (ii) point to H-bond enhancement of the rate of the $^{1}O_{2}$ reaction with Pr on the P_{SiMe} surface, but not P_{SiOH} surface. This line of thought is also supported theoretically with DFT.

(iii) DFT results show the OH group of Pr forms an H-bond in the unsymmetrical perepoxide A with an O1-C2' bond distance of 2.114 Å, an O1-C3' bond distance of 2.186 Å, and a relatively linear O-H---O1 bond angle of 167.0°. This H-bond assistance in TSB/1 enables O3' closure, forming the dihydrofuran ring in 1. The particle hydrophobicity enables an interconversion between Pr and a novel iso-hydroperoxide intermediate **B** that provides a key path in the chemistry which then follows. Formation of allylic hydroperoxides is unlikely from a ¹O₂ 'ene' reaction. Instead, dihydrofuran arises from an iso-hydroperoxide due to an intramolecular hydroxy directing ${}^{1}O_{2}$ process. Our DFT results point to the importance of a phenol O–H--- π prenyl (soft intramolecular H-bond) in Pr, that facilitates the formation of the iso-hydroperoxide B, presumably through O–H---¹O₂ hydrogen bonding. Steering effects of ¹O₂ by hydroxy groups have been reported^{45–48} and can lead to shallow minima, in which the presence of a water interface^{7,8} or confinement effects⁴⁹ perturb the 'ene' reaction. It can be noted that alcohol groups offer two distinct, if not opposite, functions in ¹O₂ chemistry. Alcohols lead to facile conversion of ¹O₂ to 3O_2 by physical quenching via electronic (E) \rightarrow vibronic (V) energy transfer $^{50-54}$ thereby shortening ¹O₂'s lifetime in protic media. On the other hand, alcohols can serve to H-bond and steer ¹O₂ to a reaction site^{55,56} provided its lifetime is long enough for the reaction; that is, it reacts prior to being physically quenched. Until now, the role of alcohol substituents on alkenes with ¹O₂ has mainly been understood for these physical quenching and H-bonding phenomena. A new mechanism outlined here points to a phenol H-bond assistance in converting a sidechain prenyl group to dihydrofuran. DFT results provide support for a mechanism of attack of phenol OH, with ¹O₂ as a key step leading to the dihydrofuran product.

Conclusion

While interfacial selectivity of ¹O₂ has been studied for years, it is not as well-appreciated with ¹O₂ as an airborne species reacting at an air-solid interface. We observed an increase in product formation on the hydrophobic nanoparticles compared to the hydrophilic nanoparticles. This product formation is in line with the ASI-k_T values of airborne ¹O₂ reacting with Pr on hydrophobic nanoparticles and hydrophilic loaded which was increased in the former. While the present particle system is static, studies of turbulent flow over the nanoparticles to potentially increase ¹O₂ would be worthwhile for future studies. The air-solid interface is probed by the new SIM method via direct phosphorescence measurements providing mechanistic insight to the interaction of ¹O₂ not only by the surface, but also in quenching of Pr on the surface. The SIM method is a novel technology to help to dissect information on partial surface association of ¹O₂ as a "transitional" gaseous-to-surface species. The SIM method can distinguish gaseous and surface-adhered ¹O₂, as state-of-the-art to fill a gap in the current knowledge of reactive species at interfaces. With the SIM analysis, mechanistic questions can now be answered at the junction of the ¹O₂'s existence. What has yet to be explored are more potent quenchers than Pr residing on particles to reach below $\theta = 91^{\circ}$ to the theoretical limit of 90°. Studies of higher surface ${}^{1}O_{2}$ quenching of polyenes than O–H solvent would support this notion.⁵⁷ The work also reveals–for the first time—an iso-hydroperoxide intermediate and that it relates to Pr selectivity in ¹O₂ chemistry. A diminished θ would also be expected of airborne ${}^{1}O_{2}$ at a water interface. With the use of eq 2-5, data from an ${}^{1}\text{O}_{2}$ air/water bubbling system 58 suggest θ in the high ninety degrees, but this type of air/water θ analysis remains to be fully examined. Future experiments could take advantage of the SIM method at the air/water interface given wide interests in the area. 59-61 SIM

analyses would enable an important photochemistry process in interfacial chemistry, including

hydrophobic waste compounds/plastics residing on ocean surfaces.

Supporting Information is available, which includes NMR spectra of products desorbed from

the reaction of airborne ¹O₂ with Pr on nanoparticles (Figures S1-S4), IR data collected on the

hydrophobic nanoparticles (Figure S5), use of an alternate slope intersection method (Figure S6),

phosphorescence spectra of ¹O₂ under different conditions (Figure S7), details pertaining to

molecule-to-molecule distance calculations, percent of surface area covered, supporting equations

S1-S3, supporting Table S1, and descriptions of energies and geometries of stationary points.

AUTHOR INFORMATION

Corresponding Author

agreer@brooklyn.cuny.edu

ORCID

Andrés M. Durantini: 0000-0002-7898-4033

Lloyd Lapoot: 0000-0001-6888-2626

Shakeela Jabeen: 0000-0002-7153-3379

Goutam Ghosh: 0000-0002-2021-4589

Johirul Bipu: 0009-0004-3384-1057

Serah Essang: 0000-0001-5640-9508

29

Alexander Greer: 0000-0003-4444-9099

Acknowledgements

We thank the National Science Foundation (CHE-2154133) for funding. This work used

Expanse in the Extreme Science and Engineering Discovery Environment (XSEDE) cluster and

Advanced Cyberinfrastructure Coordination Ecosystem: Services & Support (ACCESS) at the San

Diego Supercomputer Center, which is supported by the NSF (ACI-1548562) through allocation

CHE-210052. We thank Leda Lee for the graphic arts work and Oliver Turque for comments.

A.M.D. also acknowledges support from a Fulbright-CONICET fellowship. We also thank

Gonzalo Cosa for access to his laboratory where the steady-state ¹O₂ spectra collected in Figure

S7 (Supporting Information).

REFERENCES

1. Lissi, E. A.; Encinas, M. V.; Lemp, E.; Rubio, M. A. Singlet Oxygen $O_2(^1\Delta_g)$ Bimolecular

Processes. Solvent and Compartmentalization Effects. Chem. Rev. 1993, 93, 699-723.

2. Shiraishi, Y.; Kimata, Y.; Koizumi, H.; Hirai, T. Temperature-Controlled

Photooxygenation with Polymer Nanocapsules Encapsulating an Organic Photosensitizer.

Langmuir **2008**, 24, 9832-9836.

3. Samanta, S. R.; Choudhury, R.; Ramamurthy, V. Photoisomerization and

Photooxygenation of 1,4-Diaryl-1,3-dienes in a Confined Space J. Phys. Chem. A

2014, *118*, 10554-10562.

30

- 4. Ramamurthy, V. Photochemistry in a Capsule: Controlling Excited State Dynamics via Confinement. *Chem. Comm.* **2022**, *58*, 6571-6585.
- 5. Malek, B.; Lu, W.; Mohapatra, P.; Walalawela, N.; Jabeen, S.; Liu, J.; Greer, A. Probing the Transition State-to-Intermediate Continuum: Mechanistic Distinction between a Dry versus Wet Perepoxide in the Singlet Oxygen "Ene" Reaction at the Air–Water Interface. *Langmuir* **2022**, *38*, 6036–6048.
- Choudhury, R.; Greer, A. Synergism Between Airborne Singlet Oxygen and a Trisubstituted Olefin Sulfonate for the Inactivation of Bacteria. *Langmuir* 2014, 30, 3599-3605.
- 7. Malek, B.; Fang, W.; Abramova, I.; Walalawela, N.; Ghogare, A.; Greer, A. Ene Reactions of Singlet Oxygen at the Air-Water Interface. *J. Org. Chem.* **2016**, *81*, 6395-6401.
- 8. Jabeen, S.; Farag, M.; Malek, B.; Choudhury, R.; Greer, A. A Singlet Oxygen Priming Mechanism: Disentangling of Photooxidative and Downstream Dark Effects. *J. Org. Chem.* **2020**, *85*, 12505–12513.
- 9. Jabeen, S. Ph.D. Thesis: The Graduate Center, City University of New York, June 2022.
- 10. Durantini, A. M.; Greer, A. Interparticle Delivery and Detection of Volatile Singlet Oxygen at Air/solid Interfaces. *Environ. Sci. Technol.* **2021**, *55*, 3559–3567.
- 11. Panagiota, S.; Fotou, E.; Moussis, V.; Tsikaris, V.; Louloudi, M. Control of Tyrosyl Radical Stabilization by SiO₂-Oligopeptide Hybrid Biomimetic Materials. *Langmuir* **2022**, *38*, 9799-9809.
- 12. Toum Terrones, Y.; Torresán, M. F.; Mirenda, M.; Rodríguez, H. B.; Wolosiuk, A. Photoactive Red Fluorescent SiO₂ Nanoparticles Based on Controlled Methylene Blue Aggregation in Reverse Microemulsions. *Langmuir* **2022**, *38*, 6786-6797.

- 13. Saito, Y.; Wang, L.; Zheng, P.; Bian, P.; McCarthy, T. J. A Different Silica Surface: Radical Oxidation of Poly(methylsilsesquioxane) Thin Films and Particles (Tospearl). *Langmuir* 2020, 36, 10110-10119.
- 14. Fudickar, W.; Linker, T. Novel Anthracene Materials for Applications in Lithography and Reversible Photoswitching by Light and Air. *Langmuir* **2010**, *26*, 4421-4428.
- 15. Fudickar, W.; Linker, T. Photoimaging with Singlet Oxygen at the Solid-Air Interface *Langmuir* **2009**, *25*, 9797-9803.
- 16. Bogler, S.; Daellenbach, K. R.; Bell, D. M.; Prevot, A. S. H.; El Haddad, I.; Borduas-Dedekind, N. Singlet Oxygen Seasonality in Aqueous PM10 is Driven by Biomass Burning and Anthropogenic Secondary Organic Aerosol. *Environ. Sci. Technol.* 2022, *56*, 15389-15397.
- 17. Li, Q,; Zhao, J.; Shang, H.; Ma, Z.; Cao, H.; Zhou, Y.; Li, G.; Zhang, D.; Li, H. Singlet Oxygen and Mobile Hydroxyl Radicals Co-operating on Gas-Solid Catalytic Reaction Interfaces for Deeply Oxidizing NO_x. *Environ. Sci. Technol.* **2022**, *56*, 5830-5839.
- 18. Zhou, Y.; Chang, C.; Liu, Z.; Zhao, Q.; Xu, Q.; Li, C.; Chen, Y.; Zhang, Y.; Lu, B. Hyaluronic Acid-Functionalized Hollow Mesoporous Silica Nanoparticles as pH-Sensitive Nanocarriers for Cancer Chemo-Photodynamic Therapy. *Langmuir* **2021**, *37*, 2619-2628.
- Krajczewski, J.; Rucińska, K.; Townley, H. E.; Kudelski, A. Role of Various Nanoparticles in Photodynamic Therapy and Detection Methods of Singlet Oxygen. *Photodiag*. *Photodyn. Ther.* 2019, 26, 162–178.
- 20. Manfrin, A.; Nizkorodov, S. A.; Malecha, K. T.; Getzinger, G. J.; McNeill, K.; Borduas-Dedekind, N. Reactive Oxygen Species Production from Secondary Organic Aerosols: The Importance of Singlet Oxygen. *Environ. Sci. Technol.* 2019, *53*, 8553–8562.

- 21. Ge, M.; Tong, S.; Wang, W.; Zhang, W.; Chen, M.; Peng, C.; Li, J.; Zhou, L.; Chen, Y.; Liu, M. Important Oxidants and Their Impact on the Environmental Effects of Aerosols. *J. Phys. Chem. A* **2021**, *125*, 3813-3825.
- 22. Altinok, E.; Friedle, S.; Thomas, S. W. Furan-Containing Singlet Oxygen-Responsive Conjugated Polymers. *Macromolecules* **2013**, *46*, 756-762.
- 23. Ruetten, S. A.; Thomas, J. K. Reactions of Pyrene Excited States with Oxygen on the Surface of Porous Silica Gel and Similar Surfaces. *J. Phys. Chem. B*, **1999**, *103*, 1278–1286.
- 24. Ruzzi, M.; Sartori, E.; Moscatelli, A.; Khudyakov, I. V.; Turro, N. J. Time-Resolved EPR Study of Singlet Oxygen in the Gas Phase. *J. Phys. Chem. A* **2013**, *117*, 5232-5240.
- 25. Wang, K.-K.; Song, S.; Jung, S.-J.; Hwang, J.-W.; Kim, M.-G.; Kim, J.-H.; Sung, J.; Lee, J.-K.; Kim, Y.-R. Lifetime and Diffusion Distance of Singlet Oxygen in Air under Everyday Atmospheric Conditions. *Phys. Chem. Chem. Phys.* **2020**, *22*, 21664–21671.
- 26. Wang, Y.; Wu, J.; Xia, P. Synthesis of 1,1-dimethyl-4-indanol derivatives. *Synth. Commun.* **2006**, *36*, 2685–2698.
- 27. Durantini, A. M.; Greene, L. E.; Lincoln, R.; Martinez, S. R.; Cosa, G. Reactive Oxygen Species Mediated Activation of a Dormant Singlet Oxygen Photosensitizer: From Autocatalytic Singlet Oxygen Amplification to Chemicontrolled Photodynamic Therapy. *J. Am. Chem. Soc.* **2016**, *138*, 1215-1225.
- 28. Han, P.; Bartels, D. M. Temperature Dependence of Oxygen Diffusion in H₂O and D₂O. *J. Phys. Chem.* **1996**, *100*, 5597–5602.

- 29. Skovsen, E.; Snyder, J. W.; Lambert, J. D. C.; Ogilby, P. R. Lifetime and Diffusion of Singlet Oxygen in a Cell. *J. Phys. Chem. B* **2005**,*109*, 8570–8573.
- Frisch, M. J.; Trucks, G. W.; Schlegel, H. B.; Scuseria, G. E.; Robb, M. A.; Cheeseman, J. R.; Scalmani, G.; Barone, V.; Petersson, G. A.; Nakatsuji, H., et al. *Gaussian 16*, Revision C.01; Gaussian, Inc.: Wallingford, CT, 2016.
- 31. Dennington, R.; Keith, T.A.; Millam, J.M. *GaussView 6.0*, Semichem Inc.; Shawnee Mission, KS, 2016.
- 32. Lee, T. J.; Taylor, P. R. A Diagnostic for Determining the Quality of Single-reference Electron Correlation Methods. *Int. J. Quantum Chem.: Quantum Chem. Symp.* **1989**, *23*, 199-207.
- 33. Hanwell, M. D.; Curtis, D. E.; Lonie, D. C.; Vandermeersch, T.; Zurek, E.; Hutchison, G.
 R. Avogadro: An Advanced Semantic Chemical Editor, Visualization, and Analysis
 Platform. J. Cheminformatics 2012, 4, 17.
- 34. Jabeen, S.; Ghosh, G.; Lapoot, L.; Durantini, A. M.; Greer, A. Sensitized Photooxidation of *ortho*-Prenyl Phenol: Biomimetic Dihydrobenzofuran Synthesis and Total ¹O₂ Quenching. *Photochem. Photobiol.* **2023**, *99*, 637-641.
- 35. Bartusik, D.; Aebisher, D.; Lyons, A. M.; Greer, A. Bacterial Inactivation by a Singlet Oxygen Bubbler: Identifying Factors Controlling the Toxicity of ¹O₂ Bubbles. *Environ. Sci. Technol.* **2012**, *46*, 12098-12104.
- 36. Eisenberg, W. C.; Snelson, A.; Butler, R.; Taylor, K.; Murray, R. W. Gas Phase Generation of O₂ (¹Δ_g) at Atmospheric Pressure by Direct Laser Excitation. *J. Photochem.* **1984**, *25*, 439-448.

- 37. Sunday, M. O.; Sakugawa, H. A Simple, Inexpensive Method for Gas-phase Singlet Oxygen Generation from Sensitizer-impregnated Filters: Potential Application to Bacteria/virus Inactivation and Pollutant Degradation. *Sci. Total Environ.* **2020**, *746*, 141186.
- 38. Wang, K.-K.; Song, S.; Jung, S.-J.; Hwang, J.-W.; Kim, M.-G.; Kim, J.-H.; Sung, J.; Lee, J.-K.; Kim, Y.-R. Lifetime and Diffusion Distance of Singlet Oxygen in Air Under Everyday Atmospheric Conditions. *Phys. Chem. Chem. Phys.* **2020**, *22*, 21664-21671.
- 39. Collins, R. J.; Husain, D.; Donovan, R. J. Kinetic and Spectroscopic Studies of O₂ (¹Δ) by Time-resolved Absorption Spectroscopy in the Vacuum Ultra-violet. *J. Chem. Soc. Faraday Trans.* 2 **1973**, *69*, 145-157.
- 40. Wild, E.; Klingshirn, H.; Maier, M. Relaxation of the ¹Δ_g State in Pure Liquid Oxygen and in Liquid Mixtures of ¹⁶O₂ and ¹⁸O₂. *J. Photochem.* **1984**, *25*, 131-143.
- 41. Kearns, D. R. Physical and Chemical Properties of Singlet Molecular Oxygen. *Chem. Rev.* **1971**, *71*, 395-427.
- 42. Singleton, D. A.; Hang, C.; Szymanski, M. J.; Meyer, M. P.; Leach, A. G.; Kuwata, K. T.; Chen, J. S.; Greer, A.; Foote, C. S.; Houk, K. N. Mechanism of Ene Reactions of Singlet Oxygen. A Two-Step No-Intermediate Mechanism. *J. Am. Chem. Soc.* **2003**, *125*, 1319–1328.
- 43. Sheppard, A. N.; Acevedo, O. Multidimensional Exploration of Valley–Ridge Inflection Points on Potential-Energy Surfaces. *J. Am. Chem. Soc.* **2009**, *131*, 2530–2540.

- 44. Griesbeck, A. G.; Goldfuss, B.; Jäger, C.; Brüllingen, E.; Lippold, T.; Kleczka, M. Strong Asymmetry in the Perepoxide Bifurcation Mechanism: The Large-Group Effect in the Singlet Oxygen Ene Reaction with Allylic Alcohols. *ChemPhotoChem* **2017**, *1*, 213–221.
- 45. Adam, W.; Bottke, N.; Krebs, O.; Lykakis, I.; Orfanopoulos, M.; Stratakis, M. Ene Reaction of Singlet Oxygen, Triazolinedione, and Nitrosoarene with Chiral Deuterium-Labeled Allylic Alcohols: The Interdependence of Diastereoselectivity and Regioselectivity Discloses Mechanistic Insights into the Hydroxy-group Directivity. *J. Am. Chem. Soc.* **2002**, *124*, 14403–14409.
- 46. Dussault, P. H.; Schultz, J. A. Diastereoselective Addition of Singlet Oxygen to Highly Functionalized Z-Allylic Alcohols: Effect of Neighboring Functional Groups. J. Org. Chem. 1999, 64, 8419–8422.
- 47. Adam, W.; Brünker, H. G. Diastereoselective and Regioselective Photooxygenation of a Chiral Allylic Amine and Its Acyl Derivatives: Stereochemical Evidence for a Steering Effect by the Amino Group in the Ene Reaction of Singlet Oxygen. *J. Am. Chem. Soc.* **1993**, *115*, 3008–3009.
- 48. Griesbeck, A. G.; Adam, W.; Bartoschek, A.; El-Idreesy, T. Photooxygenation of Allylic Alcohols: Kinetic Comparison of Unfunctionalized Alkenes with Prenol-Type Allylic Alcohols, Ethers and Acetates. *Photochem. Photobiol. Sci.* **2003**, *2*, 877–881.
- 49. Natarajan, A.; Kaanumalle, L. S.; Jockusch, S.; Gibb, C. L.; Gibb, B. C.; Turro, N. J.; Ramamurthy, V. Controlling Photoreactions with Restricted Spaces and Weak Intermolecular Forces: Exquisite Selectivity During Oxidation of Olefins by Singlet Oxygen. J. Am. Chem. Soc. 2007, 129, 4132–4133.

- 50. Schweitzer, C.; Schmidt. R. Physical Mechanisms of Generation and Deactivation of Singlet Oxygen. *Chem. Rev.* **2003**, *103*, 1685–1758.
- 51. Bartusik, D.; Minnis, M.; Ghosh, G.; Greer, A. Autocatalytic-Assisted Photorelease of a Sensitizer Drug Bound to a Silica Support. *J. Org. Chem.* **2013**, *78*, 8537–8544.
- 52. Bartusik, D.; Aebisher, D.; Ghosh, G.; Minnis, M.; Greer, A. Fluorine End-Capped Optical Fibers for Photosensitizer Release and Singlet Oxygen Production. *J. Org. Chem.* **2012**, 77, 4557–4565.
- 53. Poon, T.; Sivaguru, J.; Franz, R.; Jockusch, S.; Martinez, C.; Washington, I.; Adam, W.; Inoue, Y.; Turro, N. J. Temperature and Solvent Control of the Stereoselectivity in the Reactions of Singlet Oxygen with Oxazolidinone-Substituted Enecarbamates. *J. Am. Chem. Soc.* 2004, 126, 10498–10499.
- 54. Sivaguru, J.; Solomon, M. R.; Saito, H.; Poon, T.; Jockusch, S.; Adam, W.; Inoue, Y.; Turro, N. J. Conformationally Controlled (Entropy Effects), Stereoselective Vibrational Quenching of Singlet Oxygen in the Oxidative Cleavage of Oxazolidinone-Functionalized Enecarbamates Through Solvent and Temperature Variations. *Tetrahedron* **2006**, *62*, 6707–6717.
- 55. Adam, W.; Prein, M. π-Facial Diastereoselectivity in the [4 + 2] Cycloaddition of Singlet Oxygen as a Mechanistic Probe. *Acc. Chem. Res.*, **1996**, *29*, 275-283.
- 56. Liang, Z.; Zhao, W.; Wang, S.; Tang, Q.; Lam, S.-C.; Miao, Q. Unexpected Photooxidation of H-bonded Tetracene. *Org. Lett.* **2008**, *10*, 2007-2010.
- 57. Ghogare, A. A.; Greer, A. Using Singlet Oxygen to Synthesize Natural Products and Drugs. *Chem. Rev.* **2016**, *116*, 9994-10034.

- 58. Page, S. E.; Logan, J. R.; Cory, R. M.; McNeill, K. Evidence for Dissolved Organic Matter as the Primary Source and Sink of Photochemically Produced Hydroxyl Radical in Arctic Surface Waters. *Environ. Sci.: Processes Impacts* **2014**, *16*, 807–822.
- 59. Fu, H.; Ciuraru, R.; Dupart, Y.; Passananti, M.; Tinel, L.; Rossignol, S.; Perrier, S.; Donaldson, D. J.; Chen, J.; George, C., Photosensitized Production of Atmospherically Reactive Organic Compounds at the Air/Aqueous Interface. *J. Am. Chem. Soc.* **2015**, *137*, 8348-8351.
- 60. Leresche, F.; Salazar, J. R.; Pfotenhauer, D. J.; Hannigan, M. P.; Majestic, B. J.; Rosario-Ortiz, F. L. Photochemical Aging of Atmospheric Particulate Matter in the Aqueous Phase. *Environ. Sci. Technol.* **2021**, *55*, 13152-13163.
- 61. Lin, J.; Dai, Q.; Zhao, H.; Cao, Wang, T.; Wang, G.; Chen, C. Photoinduced Release of Volatile Organic Compounds from Fatty Alcohols at the Air–Water Interface: The Role of Singlet Oxygen Photosensitized by a Carbonyl Group. *Environ. Sci. Technol.* 2021, 55, 8683-8690.

Table of Contents Graphic

